Process Variation Aware OPC with Variational Lithography Modeling

Peng Yu
ECE Department
University of Texas at Austin
Austin, TX 78712
yupeng@cerc.utexas.edu

Sean X. Shi
ECE Department
University of Texas at Austin
Austin, TX 78712
sean.shi@mail.utexas.edu

David Z. Pan
ECE Department
University of Texas at Austin
Austin, TX 78712
dpan@ece.utexas.edu

ABSTRACT

Optical proximity correction (OPC) is one of the most widely used resolution enhancement techniques (RET) in nanometer designs to improve subwavelength printability. Conventional model-based OPC assumes nominal process parameters without considering process variations, due to prohibitive runtimes of lithography simulations across process windows. This is the first paper to propose a true process-variation aware OPC (PV-OPC) framework. It is enabled by the variational lithography modeling and guided by the variational edge placement error (V-EPE) metrics. Due to the analytical nature of our models, our PV-OPC is only about 2-3× slower than the conventional OPC, but it *explicitly* considers the two main sources of process variations (dosage and focus) during OPC. Thus our post PV-OPC results are much more robust than the conventional OPC ones, in terms of both geometric printability and electrical characterization under process variations.

Categories and Subject Descriptors

B.7.2 [**Hardware**]: INTEGRATED CIRCUITS—*Design Aids*; J.6 [**Computer Applications**]: COMPUTER-AIDED ENGINEERING—*Computer-aided design (CAD)*

General Terms

Algorithms, Design, Performance, Reliability

Keywords

Lithography modeling, process variation, OPC

1. INTRODUCTION

As the IC industry evolves toward higher densities and nanometer scale dimensions, the printability and process window of the finer lithographic patterns are reduced due to the fundamental limit of the microlithography systems and process variations. As for now leading IC fabs still use 193nm lithography systems to print 65nm feature size, with the aid of various and sometimes exotic tricks so called resolution enhancement techniques (RET), such as optical proximity correction (OPC), phase shift mask (PSM), off-axis illumination (OAI) and sub-resolution assist feature (SRAF) insertion. Since the 157nm lithography and other next generation lithography (NGL) systems are not likely to be in the mainstream in the near future, it is expected that more and more extensive RETs will be used to push the lithography systems to their limits [12, 16, 22, 23]. To make the lithographic challenges even worse, process variations during manufacturing, such as those from dosage and focus variations, will also affect the final product yield.

OPC is one of the most widely used RETs by simply modifying the mask patterns to improve the printability [18]. Traditional model-based OPC assumes nominal process parameters without considering process variations [4]. Some primitive attempts have been made to incorporate the process window awareness. For example, defocus aerial images, instead of in-focus aerial image, have been used in OPC software to improve process window robustness [5, 19]. But they rely on extensive lithography simulations to choose the appropriate defocus value, which is very expensive. [10] shows how to modify the OPC algorithm to consider the expected defocus from CMP-induced wafer topography. But again, the OPC is based on a certain defocus condition, without considering focus variations and dose variations. Image-log slope, as an indicator of process sensitivity to dose variations, has been used in [5, 8]. But this approach is incapable of handling focus variations. None of these attempts are aware of the entire process window during OPC. The reason is due to prohibitive runtimes of lithography simulations across the entire process window. Actually, even without considering process variations, it has been reported that model-based OPC software could run for days on multiple computers for a single design [3].

Ignoring OPC impacts or process variations could lead to erroneous timing, power and yield characterization analysis. In [24], it is shown that post-OPC silicon image based timing analysis is substantially different from that based on the drawn layout, e.g., with 36% increase in worst-case slack and significant critical path reordering. The analysis of [24] is based on OPC with the nominal process. It is expected that the difference with consideration of process variations would be even more [20]. Statistical simulation techniques are demonstrated to map the lithography variability to CD or chip timing [2, 17]. The awareness of across chip line width variations can account for as much as 40% tightening of the best-case to worst-case timing spread [9]. Therefore, it is important to make the OPC aware of the process variations.

This is the first paper to propose a *true process-variation aware OPC* (PV-OPC) framework. It is enabled by the *variational lithography modeling* and guided by the *variational edge placement error* (V-EPE) metrics. The main contributions are as follows.

- We derive a new analytical variational lithography model, which is generic to handle any focus variation and illumination scheme.

DAC 2006, July 24–28, 2006, San Francisco, California, USA.

- We obtain the close-form formulae for the variational EPE metrics, and use them to guide our PV-OPC algorithm with explicit consideration of the two main sources of process variations (exposure dose and focus variations).
- The robustness of our PV-OPC algorithm is demonstrated in terms of both the geometrical and the electrical characterizations compared to the conventional OPC.
- The runtime of our PV-OPC algorithm is only about 2-3× that of the conventional OPC due to the analytical nature of our models, so it is feasible to be used in practice.

The rest of the paper is organized as follows. Section 2 presents our analytical variational lithography modeling. Section 3 derives the closed-form formulae for the variational EPE metrics, which are used to guide our PV-OPC algorithm in Section 4. Section 5 shows the experimental results, followed by the conclusions in section 6.

2. VARIATIONAL LITHOGRAPHY MODEL (VLIM)

Great efforts have been made to control the lithography system uniformity (over space) and stability (over time). Among all the process variations, the exposure dose and focus variations are the two most important sources hard to control. Other sources of variations can be lumped into these two sources equivalently [13].

Traditional phenomenological lithography simulators (used in various OPC softwares) can be decomposed into the optics simulators, which compute the aerial image, and the photoresist simulators, which compute the print contours based on the aerial images.

In the rest of this section, a new variational lithography model is proposed. In particular, an analytical formula for the aerial image at any defocus condition is derived. The impact of dose variation on the printed contour can be handled easily once the defocus aerial image is computed.

2.1 Optics Preliminary — Hopkins Equation

The aerial image intensity can be described by the *Hopkins Equation* [1]

$$\mathcal{I}(f,g) = \iint \mathcal{T}(f'+f, g'+g; f', g') \times \mathcal{F}(f'+f, g'+g)\mathcal{F}^*(f', g')\mathrm{d}f'\mathrm{d}g'. \quad (1)$$

$\mathcal{F}(f,g)$ is the mask transmission function $F(x,y)$ in the frequency domain. $\mathcal{T}(f,g;f',g')$ is called the *transmission cross coefficient* (TCC), given by

$$\mathcal{T}(f',g';f'',g'') = \iint \mathcal{J}_{\mathrm{O}}^{-}(f,g)\mathcal{K}(f+f', g+g') \times \mathcal{K}^*(f+f'', g+g'')\mathrm{d}f\mathrm{d}g, \quad (2)$$

where $\mathcal{J}_{\mathrm{O}}^{-}(f,g)$ and $\mathcal{K}(f,g)$ is the illumination function and the projection system transfer function, respectively. The superscript * means the complex conjugation.

Denote the focal error as z and suppose the shape of the pupil is a circle (without loss of generality), $\mathcal{K}(f,g)$ can be written as

$$\mathcal{K}(f,g) = \mathcal{K}_0(f,g)e^{i\pi z(f^2+g^2)} \quad (3)$$

where

$$\mathcal{K}_0(f,g) = \begin{cases} 1 & f^2+g^2 < 1 \\ 0 & f^2+g^2 > 1 \end{cases}. \quad (4)$$

For the conventional illumination with *partially coherent factor* s, $\mathcal{J}_{\mathrm{O}}^{-}(f,g)$ is written as

$$\mathcal{J}_{\mathrm{O}}^{-}(f,g) = \begin{cases} \frac{1}{\pi s^2} & f^2+g^2 < s^2 \\ 0 & f^2+g^2 > s^2 \end{cases} \quad (5)$$

Other illuminations can be described similarly.

The aerial image at a fixed defocus value z can be computed by the method shown in [15]. When z is a random variable, a naive way is to simulate at discrete z values, which is usually infeasible in practice.

2.2 Variational Aerial Image Modeling

In this section, we derived our new analytical variational aerial image modeling. We adapt and extend the moment expansion method in [21] (which only handles fully coherent illumination) to compute defocus aerial image for arbitrary illumination schemes.

$$\mathcal{T}(f',g';f'',g'') = \sum_{n=0}^{\infty}\frac{(i\pi z)^n}{n!}\sum_{k=0}^{n}\binom{n}{k}\iint\Big((f+f')^2+(g+g')^2\Big)^k\Big(-\big((f+f'')^2+(g+g'')^2\big)\Big)^{n-k} \times\mathcal{J}_{O}^{-}(f,g)\mathcal{K}_0(f+f',g+g')\mathcal{K}_0^*(f+f'',g+g'')\mathrm{d}f\mathrm{d}g \quad (6)$$

Expand $e^{i\pi z(f^2+g^2)}$ as $\sum_{n=0}^{\infty}\frac{\left(i\pi z(f^2+g^2)\right)^n}{n!}$, plug it in (2) and use Binomial Expansion, we have (6).

That is, $\mathcal{T}(f',g';f'',g'')$ can be expanded as

$$\mathcal{T}(f',g';f'',g'') = \sum_{n=0}^{\infty} z^n\mathcal{T}_n(f',g';f'',g'') \quad (7)$$

Plug (7) into (1), we end up with the following form

$$\mathcal{I}(f,g) = \sum_{n=0}^{\infty} z^n\mathcal{I}_n(f,g), \quad (8)$$

where

$$\mathcal{I}_n(f,g) = \iint \mathcal{T}_n(f'+f, g'+g; f', g') \times \mathcal{F}(f'+f, g'+g)\mathcal{F}^*(f', g')\mathrm{d}f'\mathrm{d}g'. \quad (9)$$

Fourier transform both sides of (8), we reach the expansion form of the aerial image intensity

$$I(x,y) = \sum_{n=0}^{\infty} z^n I_n(x,y). \quad (10)$$

For binary mask or PSM with phase 0° and 180° (the mask transmission function $F(x,y)$ is always real), we can prove that all the

odd terms in (10) are equal to 0 [25]. Then we have

$$I(x,y) = \sum_{n=0}^{\infty} z^{2n} I_{2n}(x,y). \quad (11)$$

We call the above equation the *defocus aerial image expansion*. $I_n(x,y)$'s are called the variational aerial images. It is easy to see I_0 is the in-focus ($z = 0$) aerial image. The above equation tells us that the defocus aerial image can be expressed as the in-focus image plus some correction terms. When z is small and z^n ($n \geqslant 4$) is much smaller than z^2, the higher order terms can be ignored. We get the analytical formula,

$$I(x,y) \cong I_0(x,y) + z^2 I_2(x,y). \quad (12)$$

The z range where (12) holds can be decided by looking at Bossung plot examples in Figure 5. In that figure, CD is drawn as a function of the focus error and the intensity threshold. The curves show that CD is a parabola function of defocus z for any fixed threshold. (12) is valid in the region where this parabola property holds. Typical lithography simulation shows that this property holds well in a few hundred nm (bigger than the typical defocus range in IC manufacturing). Thus (12) holds.

2.3 Kernel Decomposition and Vertex Based Table-Lookup

In this section, we show how to compute I_0 and I_2 by using the table lookup method.

Decompose $\mathcal{T}_n(f', g'; f'', g'')$ and ignore the residue terms, we have

$$\mathcal{T}_n(f', g'; f'', g'') = \sum_{k=1}^{p} \sigma_{nk} \mathcal{Q}_{nk}(f', g') \mathcal{Q}^*_{nk}(f'', g''), \quad (13)$$

where σ_{nk}'s are real numbers. After some simple manipulations, we have

$$I_n(x,y) = \sum_{k=1}^{p} \sigma_{nk} \left| Q_{nk} ** F \right|^2, \quad (14)$$

where $**$ is the convolution operator and $Q_{nk}(x,y)$ (called the kernel) is the decomposition of $\mathcal{T}_n$ in the spatial domain. Then each variational aerial image can be computed by convoluting the mask transmission function with a few kernel functions. The table generation method is similar to [15]. Algorithm 1 shows how to generate the lookup tables.

Algorithm 1 Kernel decomposition and table generation

Input: Lithography Optics System Functions — the illumination function $\mathcal{J}^-_{\mathrm{O}}(f,g)$ and the projection system transfer function $\mathcal{K}(f,g)$

Output: Generate the VLIM lookup tables

1: Compute $\mathcal{T}_n$ ($n = 0, 2$) based on (6) and (7)
2: Decompose $\mathcal{T}_n$ into $\mathcal{Q}_{nk}$ terms in (13)
3: Fourier transform $\mathcal{Q}_{nk}$ into Q_{nk} (14)
4: Compute all the upper-right rectangle convolutions from Q_{nk} and write them into table format

We propose a vertex based convolution method instead of the polygon based method used in [15], because it requires less number of table lookup times as shown in the example below. Algorithm 2 shows how to compute the variational aerial images from the lookup tables. The region where $Q_{nk}(x,y)$ is non-zero is called the support region whose size is about a few times of $\frac{\lambda(1+s)}{\mathrm{NA}}$.

Algorithm 2 Vertex based table lookup

Input: The tables generated in Algorithm 1, the decomposed mask in the form of polygons

Output: Compute the variational aerial images I_0 and I_2 at the point $\mathfrak{O}$

1: Retrieve the rectangles which intersect the $\mathfrak{O}$'s support region $\mathfrak{R}$
2: Compute the vertices of the rectangle with non-zero convolution value
3: Compute the sign of the convolution of each vertex
4: Look up the tables to get the convolution values
5: Compute I_0 and I_2 at point $\mathfrak{O}$ by summing up these values

To compute the convolution $Q_{nk} ** F$ in (14) at point $\mathfrak{O}$, we need only the mask shapes overlapping Q_{nk}'s support region $\mathfrak{R}$, which in turn can be expressed as the summation of the convolution values of each mask shape (Figure 1).

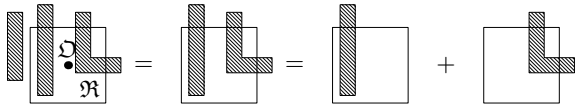

Figure 1: Mask truncation and decomposition.

For rectilinear polygons, we can compute the convolutions based on the vertices. As shown in Figure 2, any rectilinear polygon convolution can be decomposed into the summation of the convolutions of the regions to the upper-right of each vertex. We store the convolutions of all the upper-right rectangles within the support region in a look-up table for each kernel.

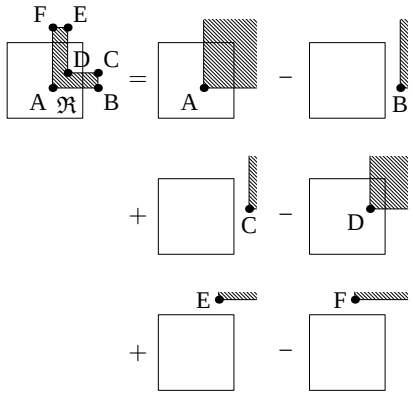

Figure 2: Vertex based rectilinear polygon convolution.

For the example in Figure 3, the contributions of B, C, E and F are zero. Only A's and D's convolutions are needed. If the method in [15] is used, four table lookups will be needed. It is clear vertex based convolution method is much better.

Both I_0 and I_2 can be computed by using this method. So the runtime of computing variational aerial images (I_0 and I_2) will be in the same order as the conventional aerial image simulation method in [15].

2.4 Threshold Bias Photoresist Model

Section 2.2 and 2.3 derive the variational aerial image modeling. The aerial image will drive the photoresist process to determine the printed image. We use the threshold bias photoresist model due

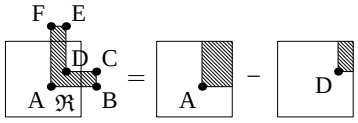

Figure 3: Look-up tables store the convolutions of all the upper-right rectangles within the support region. Convolutions with zero-contribution will not be stored.

to its simple analytical formulation. It has also been demonstrated in [7] that it predicts CD fairly accurately. This model assumes the printed contour can be computed by applying a constant bias to the contour where the intensity is equal to an intensity threshold $I_{\rm th}$. Bias and $I_{\rm th}$ can be calibrated such that the simulation correctly reproduces the CD responses to the focal error and the dose error obtained from the manufacturing measurement or more accurate photoresist simulations.

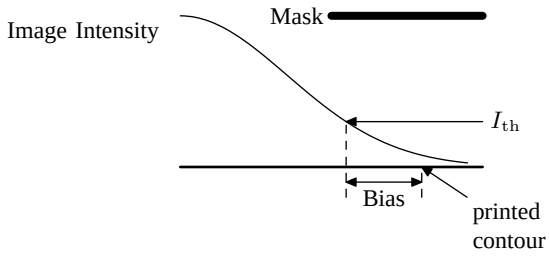

Figure 4: Threshold bias model.

3. VARIATIONAL EPE (V-EPE) METRICS

Edge Placement Error (EPE) at a given location is the distance between the print contour and the target contour. Given all EPEs along the target contour, it uniquely determines the print contour. In this section, we derive the analytical variational EPE metrics from VLIM. Our PV-OPC is based on the the variational EPE metric, while the conventional OPC is based on the nominal EPE.

3.1 Variational EPE Model

To simplify the notation, we derive the EPE (denote as E) by assuming $\mathrm{Bias} = 0$ (for general case, we only need to add the constant Bias to EPE). Since there is a one to one mapping between the intensity threshold and the exposure dose [6], we use the intensity threshold variable $I_{\rm th}$ to denote the dosage variation. Define iso-focal threshold $I_{\rm th_{iso}}$ as:

$$\left.\frac{\partial I}{\partial z}\right|_{I=I_{\rm th_{iso}}} = 0. \tag{15}$$

Since $I = I_0 + z^2 I_2$, we have

$$I_2|_{I_0=I_{\rm th_{iso}}} = 0. \tag{16}$$

So the difference between the EPE at an arbitrary process condition and the iso-focal EPE can be written as

$$E(I_{\rm th}, z) - E(I_{\rm th_{iso}}, 0) = E(I_{\rm th}, z) - E(I_{\rm th_{iso}}, z) \tag{17}$$

Approximating $E(I_{\rm th}, z) - E(I_{\rm th_{iso}}, z)$ as the following separable function [6], we have

$$E(I_{\rm th}, z) - E_{\rm iso} = a(z)b(I_{\rm th} - I_{\rm th_{iso}}), \tag{18}$$

where $b(\cdot)$ satisfies $b(0) = 0$ and $E_{\rm iso}$ is a short hand notation for $E(I_{\rm th_{iso}}, z)$. For small $I_{\rm th}$ variations (usually within 10% for modern lithography system), we have

$$E(I_{\rm th}, z) - E_{\rm iso} = a(z)(I_{\rm th} - I_{\rm th_{iso}}). \tag{19}$$

Taking the target edge $E_{\rm target}$ as the sample point, we can obtain the following variational EPE model under any intensity-threshold (equivalent to dose) and focus variation (details omitted due to space limitation)

$$E(I_{\rm th}, z) = E_{\rm iso} + a_0(1 + a_1 z^2)(I_{\rm th} - I_{\rm th_{iso}}), \tag{20}$$

where

$$\begin{cases} a_0 &= \frac{E_{\rm target} - E_{\rm iso}}{I_0(E_{\rm target}) - I_{\rm th_{iso}}} \\ a_1 &= -\frac{I_2(E_{\rm target}) - I_2(E_{\rm iso})}{I_0(E_{\rm target}) - I_{\rm th_{iso}}} \end{cases}. \tag{21}$$

3.2 Variational-EPE Metrics

From the variational EPE model (20), we can compute the V-EPE metrics of the interest to guide OPC. As an example, let us assume z and $I_{\rm th}$ are independent and normally distributed:

$$z \sim N(\mu_z, \sigma_z^2) \qquad \text{and} \qquad I_{\rm th} \sim N(\mu_{I_{\rm th}}, \sigma_{\rm th}^2), \tag{22}$$

we can compute all the EPE moments easily. Assuming $\mu_z = 0$, from (20) and (22), we have the average EPE (the first moment) under the dose and focus variations

$$\begin{aligned} \text{V-EPE} = \langle E \rangle &= E_{\rm iso} + a_0(1 + a_1\sigma_z^2)(\mu_{I_{\rm th}} - I_{\rm th_{iso}}) \\ &= E(0, I_{\rm th_{iso}}) + a_0 a_1 \sigma_z^2 (\mu_{I_{\rm th}} - I_{\rm th_{iso}}) \\ &= E_{\rm nom} + \mu_E \end{aligned} \tag{23}$$

where $E_{\rm nom}$ is the nominal EPE. It is clear that considering focus variation the average EPE $\langle E \rangle$ will be always different from the nominal EPE $E_{\rm nom}$. Note that the definition of V-EPE is not limited to the average EPE. Other desirable quantities, such as the variance, can also be included.

4. PROCESS VARIATION-AWARE OPC ALGORITHM (PV-OPC)

Conventional OPC software tries to reduce the nominal EPE. However, this would result in more post-OPC average EPE under process variations. Instead, our process variation aware OPC algorithm is based on V-EPE.

Algorithm 3 PV-OPC algorithm

Input: Non-touching polygons decomposed from the original design
Output: PV-OPCed mask

```
Segment the polygons into movable edges and tag the middle points as their control points
repeat
    updated ← false
    for each control point do
        compute the maximum aerial gradient direction
        store ⟨E⟩ along that direction
    for each edge do
        if |Const * ⟨E⟩| ⩾ manufacturing grid then
            move the edge by −Const*⟨E⟩ (rounding to a multiple of manufacturing grids)
            updated ← true
until updated = false
```

We use the standard OPC segmentation and tagging strategy [4]. Each segment is moved based on the V-EPE metric $\langle E \rangle$ at its control point. It is an iterative algorithm, where Const controls the

edge movement step. The details of the PV-OPC algorithm are shown in Algorithm 3. The main difference compared to the conventional OPC algorithm is the objective function $\langle E \rangle$ which incorporates the process-variation information. We could also use other variation-EPE metrics. Due to the analytical nature of our model and efficient table lookup, the complexity is the same as the conventional OPC, with just a slightly bigger constant (as we shall show in the experimental results)

5. EXPERIMENTAL RESULTS

5.1 The Accuracy of VLIM

We have implemented our variational lithography simulator in C++. Figure 5 shows the Focus Exposure Matrices (FEM) [14] generated by our simulator and PROLITH™ [11] at three randomly selected locations on a small binary mask with 100nm dense and iso lines. The lines and points indicate the different intensity thresholds in our model and PROLITH™ respectively. The x-axis denotes the focus error. The y-axis denote the CD. The optical parameters that we used were the partial coherence factor $s = 0.7$, the numerical aperture $\mathrm{NA} = 0.8$, the wavelength $\lambda = 193\mathrm{nm}$. It is easy to see our model CD variation prediction is consistent with PROLITH™.

5.2 OPC results comparison

We compute the CD mean and EPE variance at every 1nm in the NMOS and PMOS active regions. Then we take average of them. Table 1 shows the comparison of post-OPC average CD mean and EPE variance between conventional OPC using nominal process condition and our PV-OPC. The average CD mean from PV-OPC is much closer to 65nm than that from conventional OPC. The average EPE variance from PV-OPC are smaller as well. Thus PV-OPC is more robust with respect to process variations.

Table 1: Post-OPC CD mean and EPE variance comparison.

	average CD mean (nm)		average EPE variance (nm)	
	Conventional	PV-OPC	Conventional	PV-OPC
PMOS	61.44	65.22	3.39	3.29
NMOS	61.09	64.35	3.50	3.41

Figure 6 and 7 show the conventional OPC and PV-OPC results on an inverter poly layout according to 65nm design rules. The PMOS (upper part) channel width is 400nm the NMOS (lower part) width is 200nm. In these figures, we show the print contour at 4 typical process conditions.

Figure 6(b) shows that, the average of the two dashed lines at each sides are at the targets, but the average of the dash-dot lines tend to bias toward the center due to defocus. Figure 7(b) shows that the average of the four curves at each side are on the targets.

Figure 8 shows the robustness of PV-OPC with respect to the electrical characterizations from the post-OPC silicon image as well. Figure 8(a) shows the NMOS I-V curves at V_{gs} = 0.4V, 0.8V and 1.2V, respectively. Figure 8(b) shows the NMOS leakage current as a function of V_{gs} at $V_{\mathrm{ds}} = 1.2\mathrm{V}$. The solid curves represent the design intent of the drawn layout. The dash ones represent the post-OPC expectation of the conventional OPCed mask considering lithography variation. The dash-dot curves represent the expectation of the variation-aware OPCed mask. It is clear to see from Figure 8(a), conventional OPC can not make the I-V curve expectations the same as the design intent. However, our variation-aware OPC does a good job. Figure 8(a) shows that the sub-threshold leakage expectations of the conventional OPC results can be $3\times$

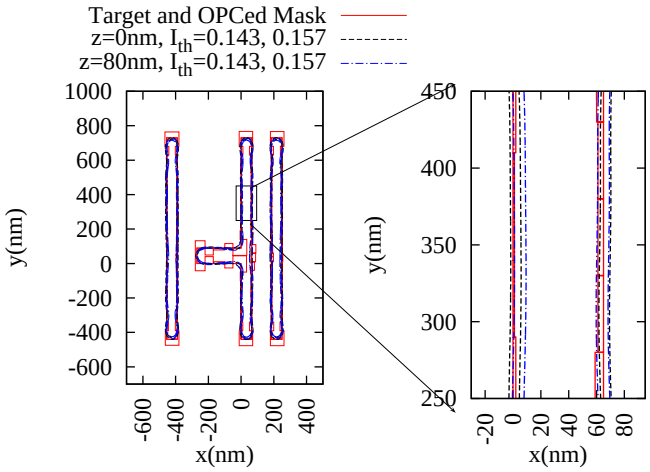

(a) Whole view (b) A zoom-in region

Figure 6: Conventional OPC (using nominal process condition as the target): the average CD error is about 5.4%

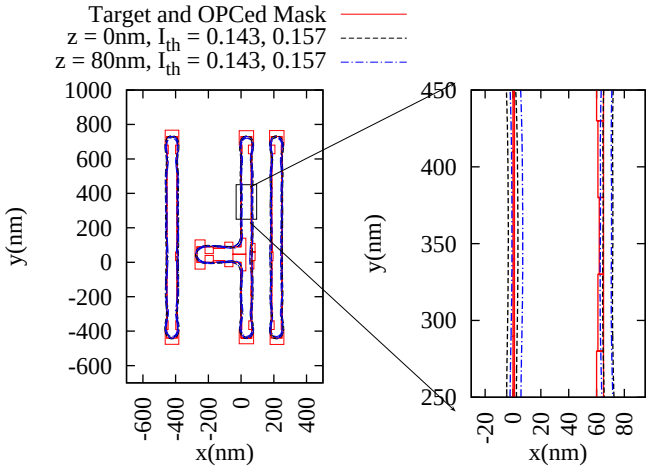

(a) Whole view (b) A zoom-in region

Figure 7: PV-OPC: the average CD error is 0.3%

bigger than the design intent. Our variation-aware OPC algorithm effectively reduces the gap.

Table 2 shows the runtime and the total number of iterations of the conventional OPC algorithm and our variation-aware OPC algorithm. Our PV-OPC runtime is only about 2-3× slower, which is very impressive considering that it explicitly incorporates the entire process window information.

Table 2: OPC Runtime Comparison

circuit	Conventional OPC		PV-OPC	
	Runtime	Iter#	Runtime	Iter#
min65	8.08s	48	20.02s	53
rec65	9.53s	50	24.16s	48

6. CONCLUSIONS

In this paper, a new variational lithography modeling is derived and its accuracy is confirmed by the industry standard simulation software PROLITH™. Base on this variational lithography model,

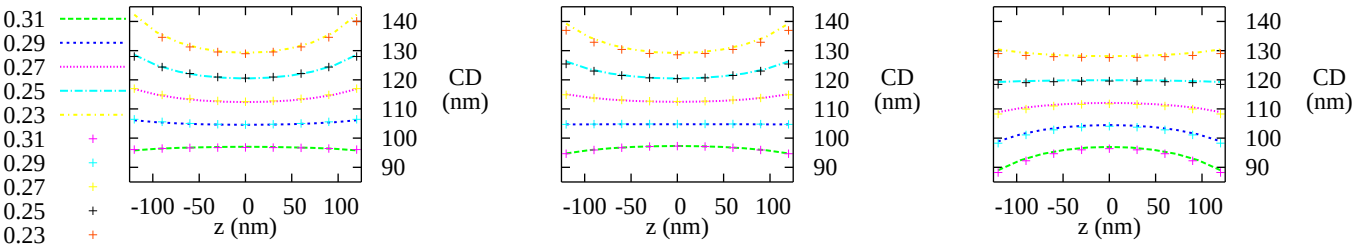

Figure 5: Bossung plots from VLIM (lines) and PROLITH^{TM}(points) at three random locations.

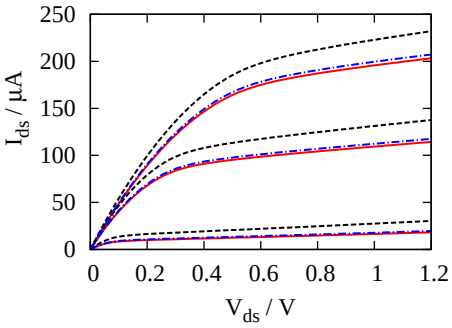

(a) *I-V* curves

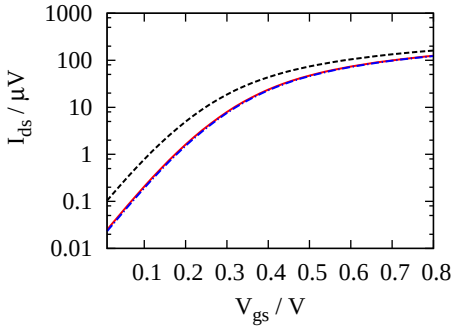

(b) Leakage (PV-OPC leakage curve is almost exact same as the design intent one)

Figure 8: NMOS electrical characterization of an inverter in 65nm technology.

the variational EPE model is presented. A variational aware OPC algorithm is proposed based on the new variational EPE metrics. The OPC algorithm is used on some 65nm layouts. Our PV-OPC obtains much more robust results than the conventional OPC in terms of both the geometric and electrical metrics. The runtime increases only 2-3×, which is very decent for a true process variation aware OPC.

7. ACKNOWLEDGMENT

This work is partially supported by SRC, IBM Faculty Award, Fujitsu, Sun, and Intel equipment donation (and software donated by KLA-Tencor). The authors would like to thank Dr. Chris Mack and Dr. Warren Grobman for helpful discussions.

8. REFERENCES

[1] M. Born and E. Wolf. *Principles of Optics : Electromagnetic Theory of Propagation, Interference and Diffraction of Light*. 7 edition.

[2] A. Borna, C. Progler, and D. Blaauw. Correlation analysis of CD-variation and circuit performance under multiple sources of variability. In *Proc. SPIE 5756*, pages 168–177, May 2005.

[3] N. Cobb and Y. Granik. New concepts in OPC. In *Proc. SPIE 5377*, pages 680–690, 2004.

[4] N. B. Cobb. *Fast Optical and Process Proximity Correction Algorithms for Integrated Circuit Manufacturing*. PhD thesis, University of California at Berkeley, 1998.

[5] N. B. Cobb and Y. Granik. OPC methods to improve image slope and process window. In *Proc. SPIE 5042*, pages 116–125, 2003.

[6] D. Fuard, M. Besacier, and P. Schiavone. Assessment of different simplified resist models. In *Proc. SPIE 4691*, pages 1266–1277, 2002.

[7] D. Fuard, M. Besacier, and P. Schiavone. Validity of the diffused aerial image model: an assessment based on multiple test cases. In *Proc. SPIE 5040*, pages 1536–1543, 2003.

[8] Y. Granik and N. B. Cobb. MEEF as a matrix. In *Proc. SPIE 4562*, pages 980–991, 2002.

[9] P. Gupta and F.-L. Heng. Toward a systematic-variation aware timing methodology. In *Proc. Design Automation Conference*, pages 321–326, 2004.

[10] P. Gupta, A. B. Kahng, C.-H. Park, K. Samadi, and X. Xu. Wafer topography-aware optical proximity correction for better DOF margin and CD control. In *Proc. SPIE 5853*, pages 844–854, 2005.

[11] KLA-Tencor. *PROLITH version 9.2*.

[12] L. Liebmann. Layout impact of resolution enhancement techniques: impediment or opportunity? In *Proc. International Symposium on Physical Design*, pages 110–117, 2003.

[13] C. A. Mack. Personal communication.

[14] C. A. Mack. *Inside PROLITH: A Comprehensive Guide to Optical Lithography Simulation*. 1997.

[15] J. Mitra, P. Yu, and D. Z. Pan. RADAR: RET-aware detailed routing using fast lithography simulations. In *Proc. Design Automation Conference*, pages 369–372, 2005.

[16] R. F. Pease. Lithographic technologies that haven't (yet) made it: lessons learned (Plenary Paper). In *Proc. SPIE 5751*, pages 15–25, 2005.

[17] C. J. Progler, A. Borna, D. Blaauw, and P. Sixt. Impact of lithography variability on statistical timing behavior. In *Proc. SPIE*, pages 101–110, 2004.

[18] C. Spence. Full-chip lithography simulation and design analysis: how OPC is changing IC design. In *Proc. SPIE 5751*, pages 1–14, 2005.

[19] J. L. Sturtevant, J. A. Torres, J. Word, Y. Granik, and P. LaCour. Considerations for the use of defocus models for OPC. In *Proc. SPIE 5756*, pages 427–436, 2005.

[20] J. L. Sturtevant, J. Word, P. LaCour, J. W. Park, and D. Smith. Assessing the impact of real world manufacturing lithography variations on post-OPC CD control. In *Proc. SPIE 5756*, pages 240–254, 2005.

[21] Y.-T. Wang, Y. C. Pati, and T. Kailath. Depth of focus and the moment expansion. *OPTICS LETTERS*, 20(18):1841–1843, Sept. 1995.

[22] A. K. Wong. Microlithography: Trends, challenges, solutions, and their impact on design. *IEEE Micro*, 23(2):12–21, 2003.

[23] A. K.-K. Wong. *Resolution Enhancement Techniques in Optical Lithography*. 2001.

[24] J. Yang, L. Capodieci, and D. Sylvester. Advanced timing analysis based on post-opc extraction of critical dimensions. In *Proc. Design Automation Conference*, pages 359–364, 2005.

[25] P. Yu, D. Z. Pan, and C. A. Mack. Fast lithography simulation under focus variations for OPC and layout optimizations. In *Proc. SPIE 6156*, pages 397–406, 2006.